Characteristics of inherent coupling structure of model climates

Xiuhua Zhu

CEN, University of Hamburg

Bundesstrasse 53, 20146 Hamburg, Germany

xiuhua.zhu@uni-hamburg.de

0049 41173 153

Early Online Release: This preliminary version has been accepted for publication in *Journal of Climate*, may be fully cited, and has been assigned DOI 10.1175/JCLI-D-20-0700.1. The final typeset copyedited article will replace the EOR at the above DOI when it is published.

Abstract

This work proposes a framework to examine interactions of climate modes that are identified as leading EOF modes; their coupling structure is unveiled through correlation analysis and helps constructing a regression model, whose performance is compared across GCMs, thereby providing a quantitative overview of model performances in simulating mode-interaction. As demonstration surface temperature is analyzed for five CMIP5 PiControl simulations. Along with the seasonal land and ocean modes, four interannual modes are identified: Tropical Mode (TM) associated with the Hadley circulation, Tropical Pacific Mode (TPM) characterizing a zonal temperature contrast between the eastern tropical Pacific and the Atlantic-Indian ocean, and two annular modes: Arctic Mode (AM) and Ant-arctic Mode (AAM). All GCMs converge on the following: 1) TM strongly couples with seasonal signals of the previous year; 2) TPM leads TM by 1 year, thus a weaker zonal temperature contrast in the tropics contributes to warming in the entire tropical band one year later; 3) AM weakly couples to TM at a one-year lead, suggesting a colder north pole may contribute to colder tropics. In addition, all GCMs do not support a linear coupling between AAM and TM. The above-learned coupling structure is incorporated to construct an optimum regression model that demonstrates considerable predictive power. The proposed approach may both serve as a useful tool for dynamical analysis and lend insight into GCM differences. Its merit is demonstrated by the finding that different representations of the mean seasonal cycle in GCMs may account for the GCM-dependence of relative contributions of seasonal and inter-annual modes to TM variability.

Accepted for publication in *Journal of Climate*. DOI10.1175/JCLI-D-20-0700.1.

38 **keywords**

39 Mode interaction, GCM, Hadley Circulation, Trans-basin connection, tropics-subtropics connec-
40 tion

41 1. Introduction

42 Global warming is drawing increasing attention largely due to a growing media coverage that often
43 associates disastrous impacts of climate extremes with anthropogenic warming. Prior to such an
44 attribution task, an essential step that has to be undertaken is to separate anthropogenically forced
45 climate signals from natural variability, which is by no means an easy task (Hasselmann 1993;
46 Hegerl and Zwiers 2011; Santer et al. 2011; Lee and Ouarda 2012; Frankcombe et al. 2015). Along
47 this way general circulation models (GCMs) become a powerful tool with increasing importance,
48 but also pose enormous challenges. This concerns model construction, validation, and projection,
49 not only in the technical sense, since it requires knowledge of computer science, mathematics and
50 climate physics, but also in the scientific sense, namely, how faithful GCMs represent key pro-
51 cesses governing the climate system.

52 On the one hand, GCM performances have been extensively evaluated regarding how key climate
53 modes and processes are reproduced, which include among many others the Hadley cell (HC) (e.g.,
54 Hu et al., 2013; Grise and Davis 2020), the Asian Monsoon system (e.g., Mishra et al. 2018; Preethi
55 et al. 2019), ENSO (e. g. Guilyardi, 2006; Chen et al. 2017; Lu et al. 2018), the Atlantic Multide-
56 cadal Oscillation and the Atlantic Meridional Overturning Circulation (Zhu et al. 2006; Drijfhout
57 et al. 2011; Weaver et al. 2012; Zhang and Wang 2013). On the other hand, model comparison has
58 seldom touched how well the interaction between climate modes is reproduced, despite a large

collection of observational and model evidences suggesting climate variability continuum (Huybers and Curry 2006; Dommenget and Latif 2008; Fraedrich et al. 2009; Lovejoy 2018), which essentially characterizes cross-scale linkages.

Take HC as an example. Some of its basic features remain challenging for GCMs. For instance, the thermodynamic structure of the HC shows significant discrepancies between models and reanalysis data (e.g., Mitas and Clement 2006). And, although there is a broad agreement between models and observations that the tropics are expanding in the recent decades, no consensus has been reached on the exact magnitude (e.g., Johanson and Fu, 2009; Hu et al., 2013; Grise and Davis 2020) and the cause of such a forced expansion (e.g., Nguyen et al., 2015; Allen and Kovilakam, 2017; Amaya et al., 2018). In addition, abundant studies reveal that the HC closely interacts with the annual cycle (e.g., Bowman and Cohen 1997; Kang and Lu 2012; Baker et al. 2018), ENSO (e.g., Oort and Yienger 1996; Quan et al. 2004), and the annular modes from both hemispheres (e.g., Previdi and Liepert 2007). Moreover, HC's response to global warming may be highly sensitive to the thermal forcing's meridional structure: when the thermal forcing is confined to a narrow region around the equator, HC contracts, which resembles its response to El-Nino events, whereas a forcing with wider meridional extent produces global warming-like HC expansion (e.g., Tandon et al. 2013; Baker et al. 2018).

All these studies suggest that GCM climates that differ in details of simulated internal climate variability and model dynamics may account for their different responses to global warming (Shepherd 2014; Staten et al. 2018). However, model-intrinsic coupling/interactions on its own, i.e., irrespective of the variation of the external forcing, have seldom been discussed, although a deep understanding about the former is prerequisite for learning about the latter, because forced responses are often projected onto the leading intrinsic modes of the climate system (e.g., Hurrel 1995; Branstator and Selton, 2009; Zhu et al. 2016).

Accepted for publication in *Journal of Climate*. DOI10.1175/JCLI-D-20-0700.1.

This study attempts to develop a framework devoted to examining interactions of the most influential climate modes in a given climate as such that it shall aid model comparison, particularly regarding how mode-interaction is represented. Within this framework, the following goals are addressed: i) to identify those climate modes that are most fundamental and active in undisturbed GCM climates; ii) to explore how these inherent climate modes couple with each other globally; and iii) to find out whether, and how, the identified coupling structure differs from one GCM to another. The focus is on inherent climate modes that are identified in global surface temperature fields through the EOF analysis, and their interactions are assessed by lead-lag correlation. Based on the identified coupling structure, a suitable regression model is introduced and applied as a model intercomparison tool to provide quantitative measures of mode interaction. A companion analysis on the coupling structure in forced simulations will be discussed separately.

This work is organized as follows: section 2 introduces data and analysis method, section 3 presents the complete analysis of the undisturbed simulation of MPI-ESM-MR (PiControl), which serves to guide the construction and selection of regression models in section 4; section 5 presents analyses of PiControl simulations of four additional GCMs and discusses the possible GCM dependence of the coupling structure; main results are summarized in section 6, and section 7 presents discussion and conclusion.

2. Data and Method

Surface temperature (ST) fields of PiControl simulations (forced by preindustrial conditions) from five CMIP5 climate models (listed in Table-1) are analyzed. First, monthly ST time series of year i and month m, $X_{i,m}$, with $i = 1 \ldots Y, m = 1 \ldots 12$, undergo a time-scale decomposition in a mathematical sense, $X_{i,m} = \overline{X}_i + X'_{i,m}$, where annual means $\overline{X}_i$ describe variations on interannual scales and monthly deviations $X'_{i,m}$ predominantly reflect the seasonal cycle and its possible change on

Accepted for publication in *Journal of Climate*. DOI10.1175/JCLI-D-20-0700.1.

longer time scales. Hereafter they are referred to as interannual and seasonal components (IAC and SC), respectively. Subsequently, these two components of the global ST fields are subjected to the correlation-matrix based EOF analysis (with area weighting considered).

The correlation-matrix based EOF analysis is applied because, in comparison to the covariance-matrix based alternative, it is less influenced by variables with stronger variability. For instance, it is well known that temperature records in polar regions have larger variances than those in lower latitudes, which is referred to as 'polar amplification' in the case of global warming (e.g. Smith et al. 2018). A covariance-matrix based EOF is expected to capture such a *contrast in genuine variability* in the first place, which is greatly mitigated by the normalization procedure (temporal anomaly divided by local standard deviation) prior to the correlation-matrix based EOF. It is expected that, through the normalization, the correlation-based EOF analysis is able to capture structures that are otherwise hidden behind the genuine structure of variances.

3. An exploratory analysis

This section first introduces EOF results of the IAC and SC in the PiControl simulation of MPI-ESM-MR. The first leading EOF mode of the IAC is selected to showcase how the coupling structure (CS) between climate modes is identified.

3.1 Interannual component (IAC)

The first IAC EOF mode (16.2% of the total variance) shows strong loadings predominantly in the tropical band and, in particular, over the tropical ocean; meanwhile, anomalies with an opposite sign occur in the mid-latitude oceans (Figure 1a). Hereafter it is referred to as the tropical mode (TM). The second and third modes (7.5% and 7.2% of the total variance), in contrast to the first

Accepted for publication in *Journal of Climate*. DOI10.1175/JCLI-D-20-0700.1.

mode that accentuates the lower latitudes, are characterized by strong temperature anomalies in either polar region (Figures 1 b-c) and referred to as the Arctic mode (AM) and the Antarctic mode (AAM), respectively. The fourth mode (5% of the total variance) (Figure 1d) is characterized on the one side by warm anomalies over the Eurasia Continent and cold anomalies over the Arctic and Canadian Archipelago and, on the other side, by trans-basin temperature gradients with negative anomalies over the Maritime continent and the tropic Atlantic and warm anomalies over the eastern tropical Pacific. As is soon to be revealed, only the trans-basin temperature gradients in the tropics interact with TM, which forms the focus of this study. Thus it is referred to as the tropical Pacific mode (TPM).

The significance of these four EOF modes is inspected with a Monte-Carlo test. Specifically, 50 subsets of 300-year ST fields are randomly selected from the entire 1000-year ST fields; each subset is subjected to the EOF analysis. It is expected that physically meaningful modes would be persistent and robust and thus retain their rank in the hierarchy. It is found that i) the match between the EOFs of the Monte-Carlo subsets and their counterparts in Figures 1a-d is evidenced by a spatial correlation of at least 0.75 in 75% of the 50 subsets (bottom edge of boxes in Figure S1-a); ii) while TM (TPM) always remains on its first (fourth) place in ranking, AM and AAM switch their ranking positions in some of the subsets, which is consistent with their explained variance being almost equal. More importantly, taking this into account, iii) the relative ranking of the four leading modes is well-kept in all Monte Carlo subsets (Figure S1-b).

Physical embedding of IAC modes

TM describes two essential aspects of the tropical circulation, i.e., the Walker cell and the Hadley cell. It characterizes a zonal contrast in sea level pressure (SLP) between the Indo-Pacific warm pool and the central and eastern tropical Pacific and depicts a negative phase of the Walker cell with sinking motion over the Maritime continent (Figure 1e). Meanwhile, its high loadings occur

Accepted for publication in *Journal of Climate*. DOI10.1175/JCLI-D-20-0700.1.

off the equator (being around 10°S and 10°N in the eastern tropical Pacific, Figure 1a) and correspond to the equinoctial pattern of the HC (Figure 1i) as has been depicted in Dima and Wallace (2003). Such an equatorially symmetric structure forms strong contrast with the seasonally-reversing solstitial pattern that associates with the monsoons (see their Figures 3-6). Stronger TM (warmer tropics) is linked with a strengthening and contraction of the HC (Figure 1i), which resembles the HC response to a narrow forcing centered at the equator (termed as El Niño–like HC contraction in Tandon et al. 2013), in contrast to the global warming like HC expansion. The latter occurs when the thermal forcing with wider meridional extent is applied (Tandon et al. 2013) and has been simulated by most CMIP GCMs under global warming (Lu et al. 2008; Lucas et al. 2014; Vallis et al. 2015).

To further substantiate the close connection of TM with warming or cooling over the *entire tropical band*, tropical mean surface temperature (averaged between 20°S and 20°N, TMT hereafter) is correlated to the TM principal component and a linear correlation of almost 1 is obtained. Next, their causal relation is examined following Liang (2014). The information flow from TMT to TM is -0.36 and that from TM to TMT is 0.54 (nats per unit time), which indicates that knowledge of TM provides *noise* (positive information flow) to TMT (thus increases its uncertainty), whereas knowledge of TMT decreases TM's uncertainty and thereby increases its predictability. Considering their close-to-1correlation coefficient, therefore, TMT as the temperature indicator of the entire tropical band is *a defining feature* of TM. In this sense, TM should be viewed as the manifestation of the Hadley circulation on surface temperature.

Both AM and AAM are characterized by a weaker pressure gradient between middle and high latitudes (Figures 1f, g) and thus correspond to negative phases of the northern and southern annular modes, respectively (Marshall 2003; Gillet et al. 2006). One interesting feature worth noting is that

Accepted for publication in *Journal of Climate*. DOI10.1175/JCLI-D-20-0700.1.

AM features cold high-pressure anomalies over the Arctic, whereas AAM features warm high pressure-anomalies over the Antarctic.

In comparison to TM, TPM also features a similar zonal contrast in SLP in the tropics (Figure 1h), but its expression in the meridional mass stream function is considerably weaker (Figure 1j). Meanwhile, its strong loadings in high latitudes (Figure 1d) suggest a possible signal mixture, which more likely occurs to lower-ranked EOF modes, because the lower the rank of one eigenvalue, the more modes that are required to be orthogonal to, and the more likely its pattern is dictated by mathematical constraints, rather than by physical or dynamical causes.

In order to explore what is more essential for the TPM, its loading in high latitudes or the zonal temperature/SLP gradients in the tropics, the EOF analysis is applied to ST fields taken from two subdomains: North of 40°N and the tropical band between 30°S and 30°N. The first leading EOF mode of the two subdomain analyses shows high spatial similarity to AM and TM, respectively, with spatial and temporal correlations of almost 1. The second mode in both cases corresponds well to TPM spatially (spatial correlation coefficients: 0.9 and 0.96) and also temporarily (both with a temporal correlation of 0.69). Therefore, they jointly capture the spatial features of TPM in high and low latitudes (Figure 1d). Their principle components are correlated to that of TM. As is soon to be discussed in section 3.3, TPM leads TM by 1 year with a strong positive correlation coefficient, which, as an indication of mode interaction, is unambiguously captured *only* by the TPM features in the tropics (Figure S2). Therefore, it is the trans-basin temperature/SLP gradient in the tropics that is engaged in the interaction between TPM and TM.

Although TM and TPM both show a similar zonal contrast in SLP in the tropical Pacific (Figures 1e, h), a discernible characteristic marks their difference: TM is characterized by an overall warming/cooling of the entire tropical band, being the weakest near the Maritime Continent. In contrast, TPM emphasizes a zonal see-saw pattern with warming/cooling in the central and eastern tropical

Accepted for publication in *Journal of Climate*. DOI10.1175/JCLI-D-20-0700.1.

Pacific and cooling/warming in the Atlantic-Indian Ocean (Figures 1a,d, Figures 1k,l), which is still visible at the upper troposphere (Figures 1m,n). Such a see-saw pattern in ST and SLP between the tropical Pacific and the Atlantic-Indian Ocean has been recognized as part of the natural variability in a prediction system and can be considerably better predicted than ENSO (Chikamoto et al. 2015; Kosaka 2018).

3.2 Seasonal component (SC)

The first two SC EOF modes account for 74.1% and 14.6% of the total variance (not shown). In order to seek a decomposition that further eases physical understanding, factor analysis is performed to rotate these two EOFs ('rotatefactors' in Matlab). Two patterns with almost equal contributions to the total variance (45% and 44%) are obtained, both showing clear inter-hemispheric temperature contrast. The first mode has strong loadings prevailingly over land, while the second one shows strong loadings mainly over the ocean (Figures 2a-b), thus hereafter they are named as the land mode (LM) and the ocean mode (OM), respectively.

In the course of a year, LM peaks in July and reaches its low in January, while approximately one month later OM reaches its high (low) in August-September (February-March) (Figure 2c). This one-to-two month delay results from the large difference in effective heat capacity between the ocean and the land.

The typical monsoon regimes deserve some special consideration here. The interplay between the two SC modes indicated by their phase difference (Figure 2c) demonstrates vividly how LM and OM work with and against each other in different months of the seasonal evolution. For instance, the earliest Asian monsoon onset (withdrawal) is reported to occur in May (September) over the Indian Peninsular and the Indo-China Peninsular (Wang and LinHo 2001). Figure 2c suggests that the early occurrence of monsoon signals in these regions may mainly result from LM that increases

Accepted for publication in *Journal of Climate*. DOI10.1175/JCLI-D-20-0700.1.

its contribution considerably in May (compared with its almost zero contribution in April); in June-August, the dominance of control shifts from LM to OM while both are still sharing the same sign and further enhance the monsoon. The subsequent withdrawal in September mainly reflects the sharp decrease of LM from August to September while OM remains more or less stable. The re-constructed climatological monthly ST field is presented in the supplement (Figure S3-a).

3.3 Coupling structure (CS)

The focus of this section is to examine how the first leading IAC mode (TM) interacts with both SC modes and IAC modes by calculating the lead-lag correlation between the corresponding prin-ciple components . Therefore, the analysis here is restricted to linear relationships.

I. TM statistics

The quantile-quantile plot (QQ-plot) suggests that TM exhibits no systematic deviation from the normal distribution (Figure 3a), which is also supported by various statistical tests for normality at 5% significance level (e.g. the Jaque-Bera test and the Anderson-Darling test, hereafter referred to as JB and AD test).

II. Cross-correlations

TM-IACs coupling: The strongest correlation is found between TM and TPM (the fourth IAC mode) when the latter leads the former by 1 year (Figure 3b). A further cross-spectrum analysis reveals strong coherence between the two at frequency of around 4, 5 and 7 years that is character-istic of ENSO periodicity (not shown). Therefore, TM and TPM jointly describe the tropical circu-lation that is strongly imprinted by ENSO dynamics. In comparison, the correlation between TM and the other two modes (AM and AAM) is much weaker, in particular, the TM-AAM correlation hardly exceeds the 95% confidence levels.

Accepted for publication in *Journal of Climate*. DOI10.1175/JCLI-D-20-0700.1.

TM-SCs coupling*:* The cross-correlation between TM and SC modes at lag -1 (SC modes lead TM by 1 year) is distinctly different from that at lag 0 and 1. The following details are noted:

i) The LM- and OM-TM correlations at lag -1 follow approximately a monotonic evolution with comparable magnitudes, i.e., the OM-TM correlation evolves from positive to negative values and has its positive (negative) extrema in January (December), while the LM-TM correlation shows a similar pathway but with opposite signs.

ii) The TM-OM correlations at lag 0 and 1 are oscillatory swinging from its negative to positive phase. The intensity extrema occur around April and October and not at the beginning and end of the year, as noted for lag -1 when it varies monotonically with time.

iii) The TM-LM correlation decreases monotonically (from positive to negative) at lag 1 and almost mirrors the pattern at lag -1, whereas at lag 0 positive correlation is found near the middle of the year (around June) and weak negative correlation in September-October. Another noteworthy feature is that the LM-TM correlation at lag 0 is considerably weaker than that of the OM, but both are of comparable magnitude at other lags.

The coupling of TM with SC modes and IAC modes at lag -1 (when they lead TM by 1 year) guides us to use this information to introduce a regression model diagnostic for TM, which is presented in the next section.

4. Regression model and its predictive quality

This section sets out in search of a combination of variables (principle components of the four IAC modes and two SC modes) to construct a regression model of TM with the highest explanatory power measured by Bayesian information criterion (BIC); the adjusted r-squared is calculated as a complementary measure.

Accepted for publication in *Journal of Climate*. DOI10.1175/JCLI-D-20-0700.1.

It is worth pointing out that BIC is selected because it measures goodness of fit, whereas another information measure, the Akaike Information Criterion (AIC), which is originally derived from a predictive view point, is more suitable for measuring predictive accuracy of a model to predict new data. For an in-depth explanation on the differences between AIC and BIC, readers are referred to Sober (2002) and Shmueli (2010).

4.1 Regression model

The regression model of TM is expressed as follows:

$$TM(t) = c + IAC^{+}(t-1) + SC^{+}(t-1, m) + \epsilon \quad (1)$$

in which *c* is a constant, ϵ is white noise with zero mean, IAC^{+} denotes the principle components of inter-annual modes and SC^{+} denotes those of the seasonal modes in month *m* of year *t-1*. Written in full expansion one obtains

$$IAC^{+}(t-1) = a_1 * TM(t-1) + a_2 * AM(t-1) + a_3 * AAM(t-1) + a_4 * TPM(t-1) \quad (2)$$

$$SC^{+}(t-1, m) = b_1 * LM(t-1, m) + b_2 * OM(t-1, m) \quad (3)$$

If only the first term on the right side of equation 2 is considered and the SC^{+} term set to zero, equation 1 represents an AR (1) model of TM.

The task here is to find out a combination of various (or all) modes that appear in equations 2 and 3 to achieve the maximum explanatory power. BIC serves as the selection criteria for the best regression model; the adjusted r-squared is also calculated as a supplementary check. Two SC modes are regarded as being inseparable because only the two together can closely capture the full seasonal cycle.

Accepted for publication in *Journal of Climate*. DOI10.1175/JCLI-D-20-0700.1.

The regression model selection is conducted in two steps:

Step-1: to examine the relative contribution of seasonal and inter-annual variability to the variability of TM (keeping only SC^+ or only IAC^+ in equation 1 in their full expansion as in equations 2 and 3). For comparison, the full regression model (SC^+ plus IAC^+ in full expansion) is also assessed. When only SC^+ is considered, the model performance is examined for each month, only the month with top performance is presented, which turns out to be December (thus m=12); this also applies to the full model.

The top performance (with the lowest BIC value) among the three regression models evaluated here turns out to be the full regression model (gray bar in Figure 4a). One also learns that the IACs-only regression model, in comparison to the SCs-only option, has a higher r-squared value and a lower BIC (BIC: 2403 vs. 2702; r2: 37% vs. 15%), suggesting a higher contribution of inter-annual modes to TM variability.

Step-2: to find the most relevant IAC modes for the regression model. Both SC modes and TM itself (term 1 in equation 2) are included by default; subsequently, all possible combinations of the remaining three IACs are added into the default model and their performances are compared. Note that the full model (SC^+ plus IAC^+ in full expansion) is listed in the last column of Figure 4b (and as well in Figure 4a).

The best performance is delivered by the regression model that excludes AAM (gray bar in Figure 4b), which is consistent with the weak and insignificant AAM-TM correlation in Figure 3b. This final optimum model, in comparison to the full regression model, has a further reduced BIC value (by 12), whereas the adjusted r-squared values of both options are almost identical and do not help distinguish them further.

Accepted for publication in *Journal of Climate*. DOI10.1175/JCLI-D-20-0700.1.

4.2 Predictive quality

A statistical model with high explanatory power is often assumed to show reasonable prediction quality, although it should be emphasized that the regression model being selected in the previous section is because of its high *explanatory power* (measured by BIC), not due to its *prediction skill* that is better measured by AIC. In fact, when using AIC as the selection criteria, the top performance regression model would be instead the full model (SC^+ plus IAC^+ in full expansion in equation 2, last column in Figures 4a, b), because AIC tends to select more general models when n is large (here n=1000) (Burnham and Anderson 2004).

To assess the prediction quality, the 1000-yr data is divided into two equal parts, the first 500 years as the training data, and the second half as holdout/validation data. Model parameters are determined from the training data (see Table 2) and kept constant for predicting the second 500 yrs.

The parameters determined from the training period lie closely to those estimated from the entire period and well within the 95% confidence intervals. The prediction shows a correlation of 0.74 with the target holdout data (Figure 5), which lies well above 0.47 that is achieved by an AR (1) model of TM.

5. GCM dependence

To explore whether the coupling structure (CS) revealed above is GCM dependent, this section is devoted to analyzing ST fields of PiControl simulations of additional four GCMs listed in Table 1. Given that the four IAC modes in MPI-ESM-MR (Figures 1a-d) correspond well to well-known climate processes with their characteristic spatial domains, they are used as orthogonal bases, onto

Accepted for publication in *Journal of Climate*. DOI10.1175/JCLI-D-20-0700.1.

which (compressed) ST fields from these four GCMs are projected, which allows *only* the information of these physically meaningful modes to be extracted; the resulting temporal loadings are then treated as principle components, from which the explained variances are calculated.

Prior to the projection, monthly ST fields are first interpolated onto the T63 grid employed in MPI-ESM-MR; their inter-annual parts are compressed (or filtered) by keeping only the first k EOF modes, k is the effective number of spatial degrees of freedom, estimated following Fraedrich et al. (1995) and Bretherton et al. (1999). The reconstructed fields with the leading k modes are then considered for projection. A brief summary on variance reduction that ensues from data compression and projection is presented in Figure S4.

The following results are noted:

1) **Normality test:** The null hypothesis that TM follows a normal distribution is rejected in NCAR-CCSM4 and GISS-E2-R (Figures 6a, j) but not in IPSL-CM5A-LR and MRI-CGCM3 (Figures 6d, g) at a 5% significance level ($P<0.01$, in AD and JB test).

2) **TM-IACs coupling**: The TM-TPM coupling at lag 1 that is observed in MPI-ESM-MR (positive correlation when TPM leading, Figure 3b) is found in all GCMs (yellow line, Figures 6 b, e, h, k) but being the weakest in IPSL-CM5A-LR (close to 0.2); the TM-AM coupling that is manifested as negative correlation at lag 1 in MPI-ESM-MR (blue line, Figure 3b) is also found in all GCMs but barely exceeding the 95% confidence levels in MRI-CGCM3 and GISS-E2-R (blue line, Figures 6b, e, h, k); the TM-AAM correlation differs from GCM to GCM being in general rather weak (red lines, Figure 6b, e, h, k).

3) **TM-SCs coupling**: MRI-CGCM3 differs greatly from the other three GCMs and is discussed separately shortly afterwards. The other three GCMs share with MPI-ESM-MR the following com-

Accepted for publication in *Journal of Climate*. DOI10.1175/JCLI-D-20-0700.1.

mon features: i) TM closely correlates to the seasonal LM (OM) that increases (decreases) monotonously at lag -1 (when SC modes leading by 1 year) with maximum intensity in December; ii) The evolution pattern at lag -1 is mirrored at lag 1, in particular, in the case of the seasonal LM; iii) at lag 0, the correlation between TM and the seasonal LM is generally weaker than that with the seasonal OM; furthermore, the TM-OM correlation at lag 0 and lag 1 distinguishes itself from that in the preceding year with an oscillatory behavior, with maximum intensity in early spring and September-October (instead of in December).

In comparison, the TM-SCs correlation is not well established in MRI-CGCM3 at all three time lags (Figure 6i), suggesting a rather limited role of seasonal components in influencing TM variability in this GCM. In NCAR-CCSM4 and GISS-E2-R the TM-SCs correlation at lag 1 (SC modes leading by 1 year) is much stronger (~ 0.6 for TM-OM and 0.4 for TM-LM in December) than that in IPSL-CM5A-LR, which hints at a larger contribution of the seasonal modes in these two model climates.

The results above are further confirmed in the regression model selection process: i) In IPSL-CM5A-LR and MRI-CGCM3, regression models that comprise only SC modes as explanatory variables ('SCs') have lower r-squared values and larger BIC than those comprising only IAC modes ('IAC(1-4)') (Figures 7b,c), suggesting a dominant contribution of IAC modes to TM variability. In contrast, ii) in NCAR-CCSM4, these two regression models ('SCs' and 'IAC(1-4)') have almost equal BIC and r-squared values, thus they make comparable contributions, whereas iii) in GISS-E2-R, seasonal modes ('SCs') make considerably larger contributions than IAC modes to TM variability. Predictions made by these selected models are presented in Figure S5.

What is common among all GCM climates is that the third IAC mode (AAM) does not help to explain TM variability, at least not in linear terms with a one-year lead. In all GCMs except GISS-

Accepted for publication in *Journal of Climate*. DOI10.1175/JCLI-D-20-0700.1.

E2-R, the optimum regression models all comprise the first, second, and fourth IAC modes (TM, AM, and TPM), whereas in GISS-E2-R only TM and TPM are included.

6. Summary

This study has proposed an approach to identify mode interaction, which in a way looks for common characteristics from different GCM climates in undisturbed PiControl simulations. Climate modes are identified by means of the EOF analysis that is applied to the inter-annual and monthly components of the ST field (IAC and SC), respectively. The lead-lag correlation between these modes serves as an indicator of mode interaction and subsequently helps to develop a regression model hierarchy that describes their interaction in a linear format. The systematic selection process for the optimum regression model not only provides an objective perspective for understanding climate dynamics but also makes it possible to quantitatively compare the coupling structure in different GCMs thereby providing hints for model improvements.

The correlation-matrix based EOF has been employed to capture patterns that are otherwise hidden behind the genuine variance contrast that is characteristic of the Earth climate, namely, i) on inter-annual time scales, large ST variation in high latitudes contrasts weak variability in the tropics, and the central and eastern tropical Pacific is loaded with considerably stronger variability than the surrounding oceans (Figure S3-b); ii) on a seasonal scale, the temperature variability over high latitude continents is much stronger than the rest of the world, particularly, in the northern Hemisphere (Figure S3-c). Owing to the correlation-matrix based EOF analysis, the leading four IAC EOF modes capture intrinsic climate modes that essentially manifest the equator-to-pole temperature gradient of the Earth climate (TM, AM, and AAM) and the zonal thermal contrast in the tropics (TPM). These modes correspond closely to well-known climate processes: i) TM characterizes a weaker (stronger) Walker cell and a stronger (weaker) Hadley circulation on interannual time

Accepted for publication in *Journal of Climate*. DOI10.1175/JCLI-D-20-0700.1.

scales. Being nearly symmetric about the equator, TM differs greatly from the cross-equatorial pattern of the Hadley circulation that associates with the monsoon systems (e.g. Dima and Wallace 2003); ii) AM and AAM correspond to the northern and southern annular modes, respectively; iii) TPM emphasizes the see-saw pattern between the eastern tropical Pacific and the Atlantic-Indian Ocean, for which the signals in the tropical Atlantic are essential. Such a pattern closely resembles the pan-tropical dipole-like SST variability that is induced by temperature anomalies in the Atlantic (Li et al. 2016) and exhibits higher predictability than ENSO (Chikamoto et al. 2015; Kosaka 2018).

It is worth stressing that it shall not be taken for granted that this set of modes necessarily comes out so clearly — it is certainly not the case, if the covariance-matrix based EOF had been used. Therefore, *being able to identify these most fundamental climate modes at once* is a vivid demonstration of the capability and usability of the proposed analysis approach. It is simple but powerful and this merit should be acknowledged accordingly.

Since these four interannual modes in the MPI-ESM climate are (geographically) cleanly separated, they serve as orthogonal bases, onto which the ST fields of other GCM simulations are projected. Such a projection allows *only* the information of the corresponding *physical* modes to be extracted so that the resulting interaction is less contaminated by mode mixing.

Factor analysis in combination with the EOF analysis captures a stable pair of seasonal modes (LM and OM), with almost equal contributions to the seasonal cycle. The one-to-two month phase lag of OM behind LM results from the seasonal variation of the incoming solar radiation and the difference in effective heat capacity between land and sea. Unlike the typical assumption of being stable and self-repeating, the seasonal cycle captured by SC modes is not constant in time (gray spread in Figure 2c) and thus suggest a modulated seasonal cycle even in undisturbed climates, which has proven to be essential for ENSO's seasonal phase locking (Wu et al. 2008; Hamlington et al. 2019).

Accepted for publication in *Journal of Climate*. DOI10.1175/JCLI-D-20-0700.1.

The following groups multi-model results into two categories:

Similarities

i) All five GCMs simulate a stronger TM (warmer tropics, stronger and contracted equinoctial cells of the HC and a weaker Walker cell) being preceded by a stronger TPM (warmer tropical Pacific and colder Atlantic-Indian ocean) by one year;

ii) Most GCMs tend to agree on a close but weak association between AM and TM: a stronger AM (colder north pole) is associated with a weaker TM (colder tropics) one year later. This correspondence is also manifested by a negative coefficient for AM (b_2<0) in statistical models (even though AM is not included into the optimum statistical model in GISS-E2-R in the end).

iii) AAM does not seem to be important for TM variability in all GCM climates, at least not in a linear format with a one-year time lag.

iv) All GCMs simulate strong coupling between seasonal modes and TM, which shows time-varying features.

When the former leads the latter by 1 year (lag -1), the correlation evolves monotonically in the annual course. Specifically, the OM-TM correlation turns from positive to negative values and has its positive (negative) extrema in January (December), while the LM-TM correlation follows a similar pathway but with opposite signs. The above feature differs completely from that at lag 0 and lag 1, in which the TM-OM correlation evolution is rather oscillatory. Another interesting feature is that the TM-LM correlation at lag 1 almost mirrors its seasonal evolution at lag -1.

Differences

Accepted for publication in *Journal of Climate*. DOI10.1175/JCLI-D-20-0700.1.

1) TM follows a normal distribution in three out of five models (IPSL-CM5A-LR, MRI-CGCM3, MPI-ESM-MR);

2) The relative contribution of the seasonal and inter-annual modes to TM variability varies greatly from GCM to GCM: in IPSL-CM5A-LR, MRI-CGCM3 and as well MP-ESM-MR, the SC contributes much less than the IAC to TM variability, while GISS-E2-R simulates the opposite and NCAR-CCSM4 simulates similar contributions from SC and IAC.

7. Discussion and conclusion

This study has focused on identifying the coupling structure that characterizes internal climate dynamics and proposed a quantitative approach to comparing the coupling structure in different GCMs. This approach makes it possible to obtain an overview on whether and how the GCM-simulated coupling structure converges or differs across models. It is unfolded in three steps, first, the most fundamental and active climate modes are identified for model climates by a correlation matrix-based EOF analysis, second, the coupling structure of these climate modes is identified by a lead-lag correlation analysis; third, the revealed correlation relationship is used to develop an optimum regression model that enables a quantitative comparison across models. The thereby gained knowledge may be envisaged as a step towards a follow-on targeted in-depth investigation into the underlying physical processes and the factors that lead to model convergence/dependence.

The results reported in this study are from GCM control simulations under preindustrial conditions. On the other hand, similar analyses of the ERA20C reanalysis data also reveal the main coupling characteristics reported here (not shown). For instance, after carefully removing the transitional trend from the reanalysis data, TM and TPM as the dominating modes in the tropics, together with AM and AAM, form the first four leading interannual (correlation-matrix based) EOF modes, which account for 16%, 8%, 7% and 5% of the total variance, respectively (36% in total); TPM

Accepted for publication in *Journal of Climate*. DOI10.1175/JCLI-D-20-0700.1.

shows its highest positive correlation with TM at a one-year lead; and the lead-lag correlation between both SCs and TM highly resembles that in Fig. 3c.

Therefore, the fact that all five GCMs simulate a strong TPM-TM coupling on inter-annual time scales provides an encouraging manifestation of model convergence on tropical dynamics. However, once seasonal variation is brought into discussion, model results tend to diverge owing to GCMs' high sensitivity to detailed structures of the simulated tropical SST that exerts strong influences on the ENSO-Hadley circulation interaction (Guilyardi 2006; Feng and Li 2013; Guo and Tan 2018 a,b; Feng et al. 2019). In fact, different relative contributions of SC and IAC modes to TM variability may relate to the model-dependent mean state and seasonal cycle (Bellenger et al. 2014), which can be seen in the seasonal statistics of the Nino34 index (Figure S6). The following features are particularly noteworthy: i) For MRI-CGCM3 the strongest warming occurs in boreal winter (instead of boreal summer); ii) For IPSL-CM5A-LR the strongest standard deviation occurs in May-June (instead of in winter months), and iii) For all GCMs except MPI-ESM-MR there exists a temperature minimum in September, which is followed by warming through December. All these features are absent in observations (Magnusson et al. 2013; Tan et al. 2020), pointing to strong model bias in simulating the very basic climatic features in the tropics, which is beyond the current scope and not discussed here. However, it may, in fact, help to explain why the relative contribution of seasonal modes to TM variability in the optimum statistical models varies from GCM to GCM (Figure 4a and Figures 7a-d).

Note that the two SC modes in Figure 2 are rotated from the leading two EOFs of the seasonal component. The current decomposition is selected because i) the interhemispheric thermal contrast that predominates in both modes is consistent with the seasonal change in the solar radiation that is irrespective of ocean or land, and ii) it clearly captures the one-to-two month lag of OM behind LM, which results from the large difference in effective heat capacity between the ocean and the

Accepted for publication in *Journal of Climate*. DOI10.1175/JCLI-D-20-0700.1.

land. It is worth pointing out that the strong correlation of TM with SC modes from December of the previous year (Figure 3c) does not depend on the eigenvector basis chosen.

The Arctic-Tropics linkage that is captured by all five GCMs has already been reported by other modelling studies (e.g. Lin et al. 2002; Jia et al. 2009; Hegyi et al. 2014; Kim and Ahn 2015; L'Heureux et al. 2017), but a clear lead-lag relationship has not yet been deciphered, which, at least partly, has to do with the choices of numerical models (e.g., atmosphere-only model or Atmosphere-Ocean coupled GCM) and initial and forcing conditions (e.g., idealized forcing for sensitivity studies or forcing directly taken from atmospheric reanalysis data) that greatly differ between studies. The Arctic-Tropics interaction has global impacts and likely involves the stratosphere - troposphere coupling and jet dynamics (e.g., Jia et al. 2009; Hegyi et al. 2014; Kim and Ahn 2015).

Indications have been found that seasonal signals are actively involved in the Arctic-Tropics connection. Below a brief introduction is presented and a more elaborated discussion is planned for a follow-on report. Specifically, in positive AM years (colder-than-normal Arctic, corresponding to negative Arctic Oscillation) the seasonal cycle is stronger than normal, which is mainly realized by the intensified land mode (LM) around its peak time, namely, in May-June-July-August and November-December, respectively (not shown). As a consequence, the Eurasian continent is anomalously warm/cold in boreal summer/winter, while in comparison, the AM-Ocean Mode (OM) correlation is notably weaker. The above feature stems from the fact that AM-related cooling /warming over the Arctic unavoidably alters the thermal contrast between the Arctic and the Eurasia continent and consequently the contrast between continents and oceans (via the strong gearing of LM and OM). Keeping in mind that in boreal winter, the Siberia-Mongolian High dwells in the cold Eurasia and dictates the strength of the East Asian winter monsoon (EAWM), by modulating the East Asian trough and the overlying jet stream. Therefore, positive AM enhances the Siberia-Mongolian High by further cooling Eurasia and consequently strengthens the EAWM. This result is consistent with

Accepted for publication in *Journal of Climate*. DOI10.1175/JCLI-D-20-0700.1.

the larger picture that emerges out of previous studies despite their different perspectives: negative Arctic Oscillation (corresponding to positive AM) being accompanied by strong Siberian High and strong EAWM (e.g., Gong et al. 2001; Wu and Wang 2002; He et al. 2017), whereby the East Asian trough and the upper-level jet stream make important contributions (Jeong and Ho 2005; Li et al. 2014; Luo and Zhang 2015; Chowdary et al. 2019). Down in the tropics, anomalously strong EAWM weakens the El Nino-related Walker circulation thus favoring La Nina conditions (Chen et al. 2000; Ma et al. 2018), which lends support to the negative sign of the AM-TM correlation reported in Fig. 3b.

Along this line, the weak loose TM-AAM connection (Fig. 3b) may relate to the weaker seasonal signals in the southern hemisphere owing to the absence of large landmass like Eurasia. This indirectly supports the vital role the seasonal component plays in the pole-tropics interaction. On the other hand, many important aspects of this coupling are not yet fully understood. For instance, how does EAWM variability interact with ENSO? Where is the key region for the interaction with the Walker Circulation, ENSO, and the Hadley circulation to take place? Is it the South China Sea, near the Maritime continents, or the Indian Ocean (Chen et al. 2000; Wang and Wu 2012; Lee and McBride, 2016)? Another piece of thought-provoking information is that, given the active role of the seasonal signal in the Arctic-Tropics connection, a quite common experiment design that involves atmosphere models forced by prescribed surface temperature patterns with a climatological seasonal cycle is doomed to miss the seasonal signal as an active player, so does the resultant mode-interaction structure. This aspect should be taken into account when interpreting the results of these sensitivity studies.

One question worth discussing concerns how TM and TPM are related to ENSO. ENSO essentially depicts abnormal conditions in the zonal temperature gradient in the tropical Pacific, where both

Accepted for publication in *Journal of Climate*. DOI10.1175/JCLI-D-20-0700.1.

TM and TPM have considerable loadings (Figures 1a, d). ENSO indicators that are retrieved locally, including area-averaged sea surface temperature in Niño regions((Trenberth and Stephaniak 2001) and the related leading EOF patterns of temperature in the tropical Pacific sector (e.g., Xu et al. 2017), unavoidably also comprise signals from TM and TPM. How to differentiate between them is rather intricate, if possible at all. For instance, both TM and TPM comprise a zonal seesaw pattern in the tropical Pacific. How to distinguish these patterns from that of ENSO has so far rarely been discussed. Such a discussion requires *unambiguous* definitions of these modes, and it concerns fundamental questions that are more of philosophical nature: *what is ENSO*? *how to define ENSO*? Moreover, TM not only links the tropics and the subtropics via the Hadley circulation but it also connects all tropical oceans through the Walker cell (Figures 1a, e, I, k, m). Therefore, its spatial scale is much larger than that of ENSO, which by definition prioritizes signals in the tropical Pacific. By focusing only on locally retrieved measures, it is almost impossible to assess to which extent TM exerts its effects on these ENSO indicators, and most likely the detected climate signals are *exclusively* attributed to ENSO.

Keeping these complications in mind, it is thus not surprising to obtain large (and statistically significant) correlation coefficients between TM/TPM and the nino34 index (not shown). In fact, the first two leading EOFs in Xu et al. (2017), which the authors refer to as *the eastern and central Pacific El Nino (EP- and CP- El Nino),* show high spatial resemblance to TM and TPM, respectively. This study suggests that their *EP-El Nino pattern* may be viewed as a manifestation of a predominant contribution of the HC (TM) within the tropical Pacific; TM mainly represents the equator-to-pole temperature gradient that drives the HC and it is of primary importance for the Earth climate (in comparison to ENSO), which provides a reasonable explanation for the much higher variances of *the EP-El Nino type* with respect to *the CP-El Nino type* (e.g., Xu et al. 2017; Freund et al. 2019).

Accepted for publication in *Journal of Climate*. DOI10.1175/JCLI-D-20-0700.1.

559 It is worthwhile mentioning that, although all five GCMs analyzed in this study are free of long-
560 term trends, it is not always the case. For this reason, some GCMs are not included in this study
561 (e.g., GFDL-CM3). In fact, the coupling structure studied here shows strong sensitivity to the trend
562 removal technique, which, while capturing most of the trend signal, also extracts part of the inher-
563 ent variability (through overfitting). This aspect will be discussed in a companion study.

564 In summarizing, this study presents how to obtain a quantitative measure of mode interaction by
565 identifying the model-intrinsic coupling structure and consequently searching the optimum statis-
566 tical model. Such an approach helps to identify those key processes that are active (or inactive) in
567 model climates. It generates an overview over model capabilities and brings insight into model
568 strengths and weaknesses, which may guide us for tasks like assigning model weights in a multi-
569 model ensemble approach. For instance, MRI-CGCM3 that simulates the weakest coupling be-
570 tween seasonal components and TM, in fact, has a strongly biased mean seasonal cycle in the trop-
571 ical Pacific which, as a sign of low profile, then justifies a low weight for MRI-CGCM3, at least
572 when seasonal variation in this region is of concern.
573

Accepted for publication in *Journal of Climate*. DOI10.1175/JCLI-D-20-0700.1.

Acknowledgement

The author wishes to acknowledge the CMIP community for providing the climate model data, retained and globally distributed in the framework of the ESGF. The CMIP data of this study were replicated and made available for this study by the DKRZ. Thanks also extend to three anonymous reviewers who helped shape this work.

References

1. Allen, R. J. and M. Kovilakam, 2017: The role of natural climate variability in recent tropical expansion. J. Climate, 30, 6329–6350, https://doi.org/10.1175/JCLI-D-16-0735.1, 2017.
2. Amaya, D. J., N. Siler, S. Xie, and A. J. Miller, 2018: The interplay of internal and forced modes of Hadley Cell expansion: lessons from the global warming hiatus. Clim. Dynam., 51, 305–319, https://doi.org/10.1007/s00382-017-3921-5, 2018
3. Baker, H. S., C. Mbengue, and T. Woollings, 2018: Seasonal sensitivity of the Hadley cell and cross-hemispheric responses to diabatic heating in an idealized GCM. Geophys. Res. Lett., 45, 2533– 2541, https://doi.org/10.1002/2018GL077013
4. Bellenger, H., E. Guilyardi, J. Leloup, M. Lengaigne, and J. Vialard, 2014: ENSO representation in climate models: from CMIP3 to CMIP5. Clim. Dyn., 42, 1999–2018, https://doi.org/10.1007/s00382-013-1783-z
5. Bowman, K. P., and P. J. Cohen, 1997: Interhemispheric Exchange by Seasonal Modulation of the Hadley Circulation. *J. Atmos. Sci.*, **54**, 2045–2059, https://doi.org/10.1175/1520-0469(1997)054<2045:IEBSMO>2.0.CO;2.
6. Branstator, G., and F. Selten, 2009: "Modes of Variability" and Climate Change. *J. Climate*, **22**, 2639–2658, https://doi.org/10.1175/2008JCLI2517.1.
7. Bretherton, C.S., M. Widmann, V.P. Dymnikov, J.M. Wallace, and I. Bladé, 1999: The Effective Number of Spatial Degrees of Freedom of a Time-Varying Field. J. Climate, **12**, 1990–2009, https://doi.org/10.1175/1520-0442(1999)012<1990:TENOSD>2.0.CO;2
8. Burnham, K. P., and D. R. Anderson, 2004: Multimodel Inference: Understanding AIC and BIC in Model Selection. Sociol. Methods Res., 33(2), 261–304, https://doi.org/10.1177/0049124104268644.

Accepted for publication in *Journal of Climate*. DOI10.1175/JCLI-D-20-0700.1.

9. Chen, C., M.A. Cane, A.T. Wittenberg, and D. Chen, 2017: ENSO in the CMIP5 Simulations: Life Cycles, Diversity, and Responses to Climate Change. J. Climate, 30, 775–801, https://doi.org/10.1175/JCLI-D-15-0901.1
10. Chen, W., H. F. Graf, and R. Huang, 2000: The interannual variability of East Asian Winter Monsoon and its relation to the summer monsoon. Adv. Atmos. Sci. 17, 48–60. https://doi.org/10.1007/s00376-000-0042-5
11. Chikamoto, Y., and Coauthors, 2015: Skilful multi-year predictions of tropical trans-basin climate variability. Nat Commun 6, 6869, https://doi.org/10.1038/ncomms7869
12. Chowdary, J.S., K. Hu, G. Srinivas, et al. 2019: The Eurasian Jet Streams as Conduits for East Asian Monsoon Variability. Curr Clim Change Rep 5, 233–244.
13. Dima, I. M., and J. M. Wallace, 2003: On the Seasonality of the Hadley Cell. *J. Atmos. Sci.*, **60**, 1522–1527, https://doi.org/10.1175/1520-0469(2003)060<1522:OTSOTH>2.0.CO;2.
14. Dommenget, D., and M. Latif, 2008: Generation of hyper climate modes. Geophys. Res. Lett., 35, L02706, doi:10.1029/2007GL031087.
15. Drijfhout, S. S., S. L. Weber, and E. van der Swaluw, 2011: The stability of the MOC as diagnosed from model projections for pre-industrial, present and future climates. Clim. Dyn., 37, 1575–1586, doi:10.1007/s00382-010-0930-z.
16. Feng, J., and J. Li, 2013: Contrasting Impacts of Two Types of ENSO on the Boreal Spring Hadley Circulation. J. Climate, 26, 4773–4789, https://doi.org/10.1175/JCLI-D-12-00298.1
17. Feng, J., J. Li, F. Jin, Z. Liu, and S. Zhao, 2019: Effect of El Niño on the response ratio of Hadley circulation to different SST meridional structures. Clim. Dyn., 53, 3877–3891, https://doi.org/10.1007/s00382-019-04756-7
18. Fraedrich, K., C. Ziehmann, and F. Sielmann, 1995: Estimates of spatial degrees of freedom. J. Climate, 8, 361–369.

Accepted for publication in *Journal of Climate*. DOI10.1175/JCLI-D-20-0700.1.

19. Fraedrich, K., R. Blender, and X. Zhu, 2009: Continuum climate variability: long-term memory, scaling, and 1/f-noise. Int. J. Mod. Phys. B, 23, 5403-5416, doi:10.1142/S0217979209063729.

20. Frankcombe, L.M., M.H. England, M.E. Mann, and B.A. Steinman, 2015: Separating Internal Variability from the Externally Forced Climate Response. J. Climate, 28, 8184–8202, https://doi.org/10.1175/JCLI-D-15-0069.1

21. Freund, M.B., B.J. Henley, D.J. Karoly, H.V. McGregor, N. J. Abram, and D. Dommenget, 2019: Higher frequency of Central Pacific El Niño events in recent decades relative to past centuries. Nat. Geosci. 12, 450–455, https://doi-org.e-bis.mpimet.mpg.de/10.1038/s41561-019-0353-3

22. Gillet, T. D. Kell, and P. D. Jones, 2006: Regional climate impacts of the southern annular mode. Geophys. Res. Lett., 33, L23704, doi:10.1029/2006GL027721.

23. Gong, D., S. Wang, and J. Zhu, 2001: East Asian Winter Monsoon and and Arctic Oscillation. Geophys. Res. Lett., 28(10) 0094-8276, https://doi.org/10.1029/2000GL012311

24. Grise, K. M., and S. M. Davis, 2020: Hadley cell expansion in CMIP6 models. Atmos. Chem. Phys., 20, 5249–5268, https://doi.org/10.5194/acp-20-5249-2020, 2020.

25. Guilyardi, E, 2006: El Niño-mean state-seasonal cycle interactions in a multi-model ensemble. Clim. Dyn., 26, 329–348.

26. Guo, Y., and Z. Tan, 2018a: Relationship between El Niño–Southern Oscillation and the Symmetry of the Hadley Circulation: Role of the Sea Surface Temperature Annual Cycle. J. Climate, 31, 5319–5332, https://doi.org/10.1175/JCLI-D-17-0788.1

27. Guo, Y., and Z.-M. Tan, 2018b: On the sensitivity of the relationship between Hadley circulation asymmetry and ENSO in CMIP5 models. Geophys. Res., 45, 9253–9259, https://doi.org/10.1029/2018GL079515

Accepted for publication in *Journal of Climate*. DOI10.1175/JCLI-D-20-0700.1.

28. Hamlington, B. D., J. T. Reager, H. Chandanpurkar, and K.-Y. Kim, 2019: Amplitude modulation of seasonal variability in terrestrial water storage. Geophys. Res., 46, 4404–4412. https://doi.org/10.1029/2019GL082272

29. Hasselmann, K., 1993: Optimal Fingerprints for the Detection of Time-dependent Climate Change. J. Climate, 6, 1957–1971, https://doi.org/10.1175/1520-0442(1993)006<1957:OFFTDO>2.0.CO;2

30. He, S., Y. Gao, F. Li, H. Wang, and Y. He, 2017: Impact of Arctic Oscillation on the East Asian climate: A review. Earth-Science Reviews, 164(48-62), https://doi.org/10.1016/j.earscirev.2016.10.014.

31. Hegerl, G., and F. Zwiers, 2011: Use of models in detection and attribution of climate change. WIREs Clim. Change, 2, 570-591, doi:10.1002/wcc.121

32. Hegyi, B.M., Y. Deng, R.X. Black, and R. Zhou, 2014: Initial Transient Response of the Winter Polar Stratospheric Vortex to Idealized Equatorial Pacific Sea Surface Temperature Anomalies in the NCAR WACCM. J. Climate, 27, 2699–2713, https://doi.org/10.1175/JCLI-D-13-00289.1

33. Hu, Y., L. Tao, and J. Liu, 2013: Poleward expansion of the Hadley circulation in CMIP5 simulations. Adv. Atmos. Sci., 30, 790–795, https://doi.org/10.1007/s00376-012-2187-4, 2013.

34. Hurrell, J. W., 1995: Decadal trends in the North Atlantic Oscillation: Regional temperatures and precipitation. Science, 269, 676–679.

35. Huybers, P., and W. Curry, 2006: Links between annual, Milankovitch and continuum temperature variability. Nature, 441, 329–332, https://doi.org/10.1038/nature04745

36. Jia, X., H. Lin, and J. Derome, 2009: The influence of tropical Pacific forcing on the Arctic Oscillation. Clim. Dyn., 32, 495–509, https://doi.org/10.1007/s00382-008-0401-y

Accepted for publication in *Journal of Climate*. DOI10.1175/JCLI-D-20-0700.1.

674 37. Jeong, J.-H., and C.-H. Ho, 2005: Changes in occurrence of cold surges over east Asia in asso-
675 ciation with Arctic Oscillation. Geophys. Res. Lett., 32, L14704, doi:10.1029/2005GL023024.
676 38. Johanson, C. M., and Q. Fu, 2009: Hadley cell widening: Model simulations versus observa-
677 tions. J. Climate, 22, 2713–2725, https://doi.org/10.1175/2008JCLI2620.1.
678 39. Kang, S. M., and J. Lu, 2012: Expansion of the Hadley Cell under Global Warming: Winter
679 versus Summer. *J. Climate*, **25**, 8387–8393, https://doi.org/10.1175/JCLI-D-12-00323.1.
680 40. Kim, H., and J. Ahn, 2015: Improvement in Prediction of the Arctic Oscillation with a Realistic
681 Ocean Initial Condition in a CGCM. J. Climate, 28, 8951–8967, https://doi.org/10.1175/JCLI-
682 D-14-00457.1
683 41. Kosaka, Y., 2018: Slow warming and the ocean see-saw. Nature Geosci.,11, 12–13,
684 https://doi.org/10.1038/s41561-017-0038-8
685 42. Lee, T., and T.B.M.J. Ouarda, 2012: An EMD and PCA hybrid approach for separating noise
686 from signal, and signal in climate change detection. Int. J. Climatol., 32: 624-634.
687 doi:10.1002/joc.2299
688 43. Li, X., S. Xie, S. T. Gille, and C. Yoo, 2016: Atlantic-induced pan-tropical climate change over
689 the past three decades. Nature Clim Change 6, 275–279, https://doi.org/10.1038/nclimate2840
690 44. Li, F., H. Wang, and Y. Gao, 2014: On the Strengthened Relationship between the East Asian
691 Winter Monsoon and Arctic Oscillation: A Comparison of 1950–70 and 1983–2012. J. Cli-
692 mate, 27(13), 5075-5091.
693 45. Liang, X. San, 2014: Unraveling the cause-effect relation between time series. Phys. Rev. E
694 90(5-1): 052150. DOI:https://doi.org/10.1103/PhysRevE.90.052150.
695 46. Lu, J., G. Chen, and D. M. W. Frierson, 2008: Response of the zonal mean atmospheric circu-
696 lation to El Niño versus global warming. J. Clim., 21, 5942–5959.

Accepted for publication in *Journal of Climate*. DOI10.1175/JCLI-D-20-0700.1.

697 47. Lu, Z., Z. Fu, L. Hua, N. Yuan, and L. Chen, 2018: Evaluation of ENSO simulations in CMIP5
698 models: A new perspective based on percolation phase transition in complex networks. Sci.
699 Rep., 8, 14912, https://doi.org/10.1038/s41598-018-33340-y
700 48. Lucas, C., B. Timbal, and H. Nguyen, 2014: The expanding tropics: a critical assessment of the
701 observational and modeling studies. WIREs Clim Change, 5: 89-112. doi:10.1002/wcc.251
702 49. Luo, X., and Y. Zhang 2015: The Linkage between Upper-Level Jet Streams over East Asia
703 and East Asian Winter Monsoon Variability. J. Climate, 28(22), 9013-9028.
704 50. L'Heureux, M. L., M. K. Tippett, A. Kumar, A. H. Butler, L. M. Ciasto, Q. Ding, and N. C.
705 Johnson, 2017: Strong relations between ENSO and the Arctic Oscillation in the North Amer-
706 ican Multimodel Ensemble. Geophys. Res., 44, 11,654–
707 11,662, https://doi.org/10.1002/2017GL074854
708 51. Lin, H., J. Derome, R. J. Greatbatch, K. Andrew Peterson, and J. Lu, 2002: Tropical links of
709 the Arctic Oscillation. Geophys. Res. Lett., 29(20), 1943, doi:10.1029/2002GL015822.
710 52. Lovejoy, S., 2018: Spectra, intermittency, and extremes of weather, macroweather and cli-
711 mate. Sci .Rep. 8, 12697, https://doi.org/10.1038/s41598-018-30829-4
712 53. Lu, Z., Z. Fu, L. Hua, N. Yuan, and L. Chen, 2018: Evaluation of ENSO simulations in CMIP5
713 models: A new perspective based on percolation phase transition in complex networks. Sci.
714 Rep., 8, 14912, https://doi.org/10.1038/s41598-018-33340-y
715 54. Ma, T., W. Chen, D. Nath, et al. 2018: East Asian Winter Monsoon Impacts the ENSO-related
716 Teleconnections and North American Seasonal Air Temperature Prediction. Sci Rep 8, 6547.
717 https://doi.org/10.1038/s41598-018-24552-3
718 55. Magnusson, L., M. Alonso-Balmaseda, and F. Molteni, 2013: On the dependence of ENSO
719 simulation on the coupled model mean state. *Clim. Dyn.* **41,** 1509–1525,
720 https://doi.org/10.1007/s00382-012-1574-y

Accepted for publication in *Journal of Climate*. DOI10.1175/JCLI-D-20-0700.1.

721 56. Marshall, G. J., 2003: Trends in the Southern Annular Mode from Observations and Reanal-
722 yses. J Climate, 16, 4134-4143.
723 57. Mishra, S.K., S. Sahany, P. Salunke, I.-S. Kang, and S. Jain, 2018: Fidelity of CMIP5 multi-
724 model mean in assessing Indian monsoon simulations. npj Clim. Atmos. Sci., 1, 39,
725 https://doi.org/10.1038/s41612-018-0049-1.
726 58. Mitas, C. M., and A. Clement, 2006: Recent behavior of the Hadley cell and tropical thermo-
727 dynamics in climate models and reanalyses. Geophys. Res. Lett., 33, L01810,
728 doi:10.1029/2005GL024406.
729 59. Nguyen, H., C. Lucas, A. Evans, B. Timbal, and L. Hanson, 2015: Expansion of the Southern
730 Hemisphere Hadley cell in response to greenhouse gas forcing. J. Climate, 28, 8067–8077,
731 https://doi.org/10.1175/JCLI-D-15-0139.1, 2015.
732 60. Oort, A. H., and J. J. Yienger, 1996: Observed Interannual Variability in the Hadley Circulation
733 and Its Connection to ENSO. *J. Climate*, **9**, 2751–2767, https://doi.org/10.1175/1520-
734 0442(1996)009<2751:OIVITH>2.0.CO;2.
735 61. Previdi, M., and B. G. Liepert, 2007: Annular modes and Hadley cell expansion under global
736 warming, Geophys. Res. Lett., 34, L22701, doi:10.1029/2007GL031243.
737 62. Preethi, B., R. Ramya, S.K. Patwardhan, M. Mujumdar, and R. H. Kripalani, 2019: Variability
738 of Indian summer monsoon droughts in CMIP5 climate models. Clim. Dyn., 53, 1937–1962,
739 https://doi.org/10.1007/s00382-019-04752-x
740 63. Quan, XW., H.F. Diaz, and M. P. Hoerling, 2004: Change in the Tropical Hadley Cell Since
741 1950. In: Diaz H.F., Bradley R.S. (eds) The Hadley Circulation: Present, Past and Future. Adv.
742 Glob. Chang. Res., 21. Springer, Dordrecht. https://doi.org/10.1007/978-1-4020-2944-8_4
743 64. Santer, B. D., and Coauthors, 2011: Separating signal and noise in atmospheric temperature
744 changes: The importance of timescale. J. Geophys. Res., 116, D22105,
745 doi:10.1029/2011JD016263.

Accepted for publication in *Journal of Climate*. DOI10.1175/JCLI-D-20-0700.1.

746 65. Shepherd, T., 2014: Atmospheric circulation as a source of uncertainty in climate change pro-
747 jections. Nature Geosci 7, 703–708, https://doi.org/10.1038/ngeo2253
748 66. Shmueli, G., 2010: To Explain or to Predict? Statist. Sci., 25 (3), 289-310.
749 67. Smith, D., and Coauthors, 2018: The Polar Amplification Model Intercomparison Project
750 (PAMIP) contribution to CMIP6: Investigating the causes and consequences of polar amplifi-
751 cation. Geosci. Model Dev.,12(3):1139-1164, DOI: 10.5194/gmd-12-1139-2019
752 68. Sober, E., 2002: Instrumentalism, parsimony, and the Akaike framework. Phil. Sci., 69, 112-
753 S123.
754 69. Staten, P.W., J. Lu, K.M. Grise, S. M. Davis, and T. Birner, 2018: Re-examining tropical ex-
755 pansion. Nature Clim Change 8, 768–775, https://doi.org/10.1038/s41558-018-0246-2
756 70. Tan, X., Y. Tang, T. Lian, Z. Yao, X. Li, and D. Chen, 2020: A study of the effects of westerly
757 wind bursts on ENSO based on CESM. Clim. Dyn., 54, 885–899,
758 https://doi.org/10.1007/s00382-019-05034-2
759 71. Tandon, N. F., E. P. Gerber, A. H. Sobel, and L. M. Polvani, 2013: Understanding Hadley Cell
760 Expansion versus Contraction: Insights from Simplified Models and Implications for Recent
761 Observations. *J. Climate*, **26**, 4304–4321, https://doi.org/10.1175/JCLI-D-12-00598.1.
762 72. Trenberth, K. E., and D. P. Stepaniak, 2001: Indices of El Niño Evolution. *J. Climate*, **14**,
763 1697–1701, https://doi.org/10.1175/1520-0442(2001)014<1697:LIOENO>2.0.CO;2.
764 73. Vallis, G.K., P. Zurita-Gotor, C. Cairns, and J. Kidston, 2015: Response of the large-scale
765 structure of the atmosphere to global warming. Q.J.R. Meteorol. Soc., 141: 1479-1501.
766 doi:10.1002/qj.2456
767 74. Wang, B., and LinHo, 2001: Rainy Season of the Asian–Pacific Summer Monsoon. J Climate,
768 15, 386-398, https://doi.org/10.1175/1520-0442(2002)015<0386:RSOTAP>2.0.CO;2.

Accepted for publication in *Journal of Climate*. DOI10.1175/JCLI-D-20-0700.1.

769 75. Wang, L., and Wu, R., 2012: In-phase transition from the winter monsoon to the summer mon-
770 soon over East Asia: Role of the Indian Ocean, J. Geophys. Res., 117, D11112,
771 doi:10.1029/2012JD017509.
772 76. Weaver, A. J., and Coauthors, 2012: Stability of the Atlantic meridional overturning circula-
773 tion: A model intercomparison. *Geophys. Res. Lett.*, 39, L20709, doi:10.1029/2012GL053763.
774 77. Wu, B., and Wang J., 2002: Winter Arctic Oscillation, Siberian High and East Asian Winter
775 Monsoon. Geophys. Res. Lett., 29 (19), 1897, doi:10.1029/2002GL015373.
776 78. Wu, Z., E.K. Schneider, B.P. Kirtman, E.S. Sarachik, N. Huang, and C. J. Tucker, 2008: The
777 modulated annual cycle: an alternative reference frame for climate anomalies. Clim.
778 Dyn. 31, 823–841, https://doi.org/10.1007/s00382-008-0437-z.

779 79. Xu, K., C. Tam, C. Zhu, B. Liu, and W. Wang, 2017: CMIP5 Projections of Two Types of El
780 Niño and Their Related Tropical Precipitation in the Twenty-First Century. *J. Climate*, **30**,
781 849–864, https://doi.org/10.1175/JCLI-D-16-0413.1.
782 80. Zhang, L., and C. Wang, 2013: Multidecadal North Atlantic sea surface temperature and At-
783 lantic meridional overturning circulation variability in CMIP5 historical simulations. *J. Ge-*
784 *ophys. Res. Oceans*, 118, 5772– 5791, doi:10.1002/jgrc.20390.
785 81. Zhu, X., K. Fraedrich, and R. Blender, 2006: Variability regimes of simulated Atlantic MOC.
786 Geophys. Res., 33, L21603, doi:10.1029/2006GL027291.
787 82. Zhu, X., J. Bye, K. Fraedrich, and I. Bordi, 2016: Statistical Structure of Intrinsic Climate Var-
788 iability under Global Warming. *J. Climate*, **29**, 5935–5947, https://doi.org/10.1175/JCLI-D-
789 15-0505.1.

Accepted for publication in *Journal of Climate*. DOI10.1175/JCLI-D-20-0700.1.

Tables

Table -1: Five PiControl GCM simulations

PiControl	MPI-ESM-MR	NCAR_CCSM4	IPSL-CM5A-LR	MRI-CGCM3	GISS-E2-R
Duration (years)	1000	1051	1000	500	550

Table-2 Parameters of the optimum regression model (AAM excluded, thus $a_3 = 0$) for the PiControl simulation of MPI-ESM-MR; LM and OM are taken from December (m=12). Numbers in parenthesis denote the 95% confidence intervals. Parameters estimated from the entire 1000-year data are listed for comparison.

MPI-ESM-MR Optimum Model	$\mathbf{b_1(LM)}$	$\mathbf{b_2(OM)}$	$\mathbf{a_1(TM)}$	$\mathbf{a_2(AM)}$	$\mathbf{a_4(TPM)}$
Entire 1000 yrs	2.01 (1.19 2.84)	-6.42 (-7.38, -5.45)	0.55 (0.50, 0.59)	-0.10 (-0.14, -0.06)	0.26 (0.21, 0.30)
First 500 yrs	1.70 (0.55, 2.84)	-6.12 (-7.49, -4.76)	0.54 (0.48, 0.61)	-0.10 (-0.17, -0.04)	0.23 (0.17, 0.30)

Accepted for publication in *Journal of Climate*. DOI10.1175/JCLI-D-20-0700.1.

Figure Legends

Figure 1: (MPI-ESM-MR) a-d) The leading four IAC EOF modes of surface temperature: TM (IAC1), AM(IAC2), AAM (IAC3), and TPM (IAC4) (unit: std of IAC, explained variances: 16.2%, 7.5%, 7.2%, 5.0%); e-h) Correlation coefficients between the corresponding principle components and sea level pressure (SLP) (shadowed are significant values at 5%); i-n) Composites (color shading) of mass streamfunction (i, j, unit: 10^9 kg/s), surface temperature (k, l, unit: K) and velocity potential at 200hPa (m, n, unit: $10^6 m^2/s$) for TM and TPM (positive minus negative); climatological fields are contoured.

Figure 2: (MPI-ESM-MR) The leading two EOF modes of the seasonal component (SC) of surface temperature: a) Land mode (SC-land) and b) Ocean mode (SC-ocean) (a-b, unit: std of SC, explained variances are 45% and 44%, respectively); c) their seasonal courses. Monthly ranges are shadowed.

Figure 3 (MPI-ESM-MR) a) Q-Q plot of the TM (IAC1) principal component: (upper panel: normal Q-Q plot; lower panel: residual Q-Q plot); b-c) Cross-correlations between PCs of TM (IAC1) and b) other IAC modes (IAC2: AM, IAC3: AAM, IAC4: TPM) and c) two seasonal modes. In b), horizontal dashed lines mark the 95% confidence intervals; in c) coefficients with $P<0.01$ are marked with squares; lag = -1corresponds to seasonal modes leading TM by 1 year; the climatological monthly cycle of two seasonal modes (blue: LM, 'SC-land', brown: OM, 'SC-ocean') follows right axis.

Figure 4 (MPI-ESM-MR) Performance of candidate statistical models in terms of BIC (left axis) and r-squared (right axis) assessed in two steps; the top performer at each step is marked in gray. a) Three regression models: *SCs-only, IAC(1-4)-only*, and *SCs+IAC(1-4)* (the full model). b) Eight regression models, all including both SCs and TM(IAC1) but with different combinations of the

Accepted for publication in *Journal of Climate*. DOI10.1175/JCLI-D-20-0700.1.

other three IAC modes (IAC 2, 3, 4). The optimum regression model turns to be *SCs+IAC(1-2, 4).* All candidate models comprising both SCs show their lowest BIC in December, thus m=12.

Figure 5 (MPI-ESM-MR) Cross-validation of the optimum regression model for the PiControl simulation, with parameters determined from the first 500 years of TM's principle component (listed in Table 2), while the rest 500-yr data serves as the target holdout data (black), with respect to which predictions (red) are compared. Correlation between the holdout data and predictions is 0.74.

Figure 6: (Multi-models) same as Fig.3 but for NCAR-CCSM4(a-c), IPSL-CM5A-R(d-f), MRI-CGCM3(g-i), and GISS-E2-R(j-l). Only residual QQ plots are shown. The null hypothesis that TM follows normal distribution is rejected in a) and j) ($p<0.01$, in both AD test and JB test).

Figure 7 (Multi-models) same as Figure 4a but including the optimum regression model in the last column (marked in gray). All regression models comprising seasonal components as explanatory variables have their best performances in December (m=12).

Accepted for publication in *Journal of Climate*. DOI10.1175/JCLI-D-20-0700.1.

Figure 1: (MPI-ESM-MR) a-d) The leading four IAC EOF modes of surface temperature: TM (IAC1), AM(IAC2), AAM (IAC3), and TPM (IAC4) (unit: std of IAC (Figure S3-b), explained variances: 16.2%, 7.5%, 7.2%, 5.0%); e-h) Correlation coefficients between the corresponding principle components and sea level pressure (SLP) (shadowed are significant values at 5%); i-n) Composites (color shading) of mass streamfunction (i, j, unit: 10^9 kg/s), surface temperature (k, l, unit: K) and velocity potential at 200hPa (m, n, unit: $10^6 m^2/s$) for TM and TPM (positive minus negative); climatological fields are contoured.

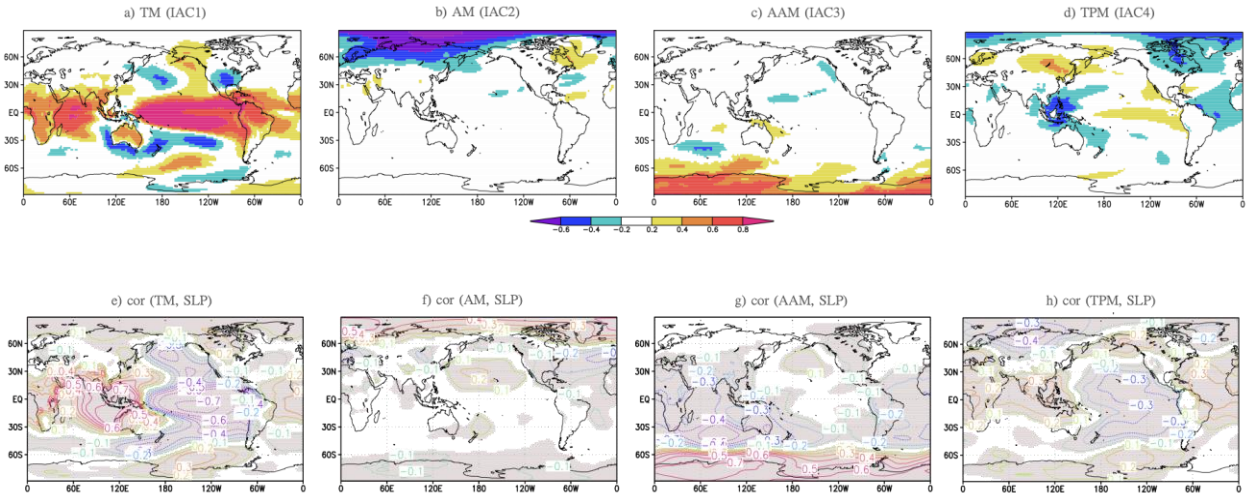

Accepted for publication in *Journal of Climate*. DOI10.1175/JCLI-D-20-0700.1.

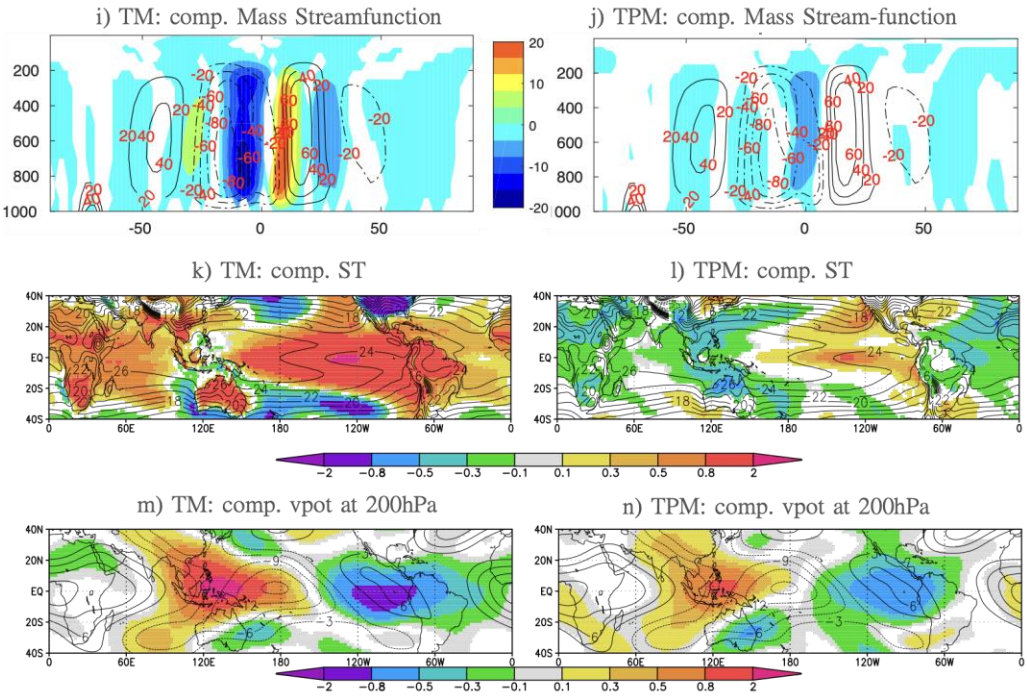

846

847

848

849

Accepted for publication in *Journal of Climate*. DOI10.1175/JCLI-D-20-0700.1.

850 Figure 2: (MPI-ESM-MR) The leading two EOF modes of the seasonal component (SC) of surface
851 temperature: a) Land mode (SC-land) and b) Ocean mode (SC-ocean) (a-b, unit: std of SC (Figure
852 S3-c), explained variances are 45% and 44%, respectively); c) their seasonal courses. Monthly
853 ranges are shadowed.
854

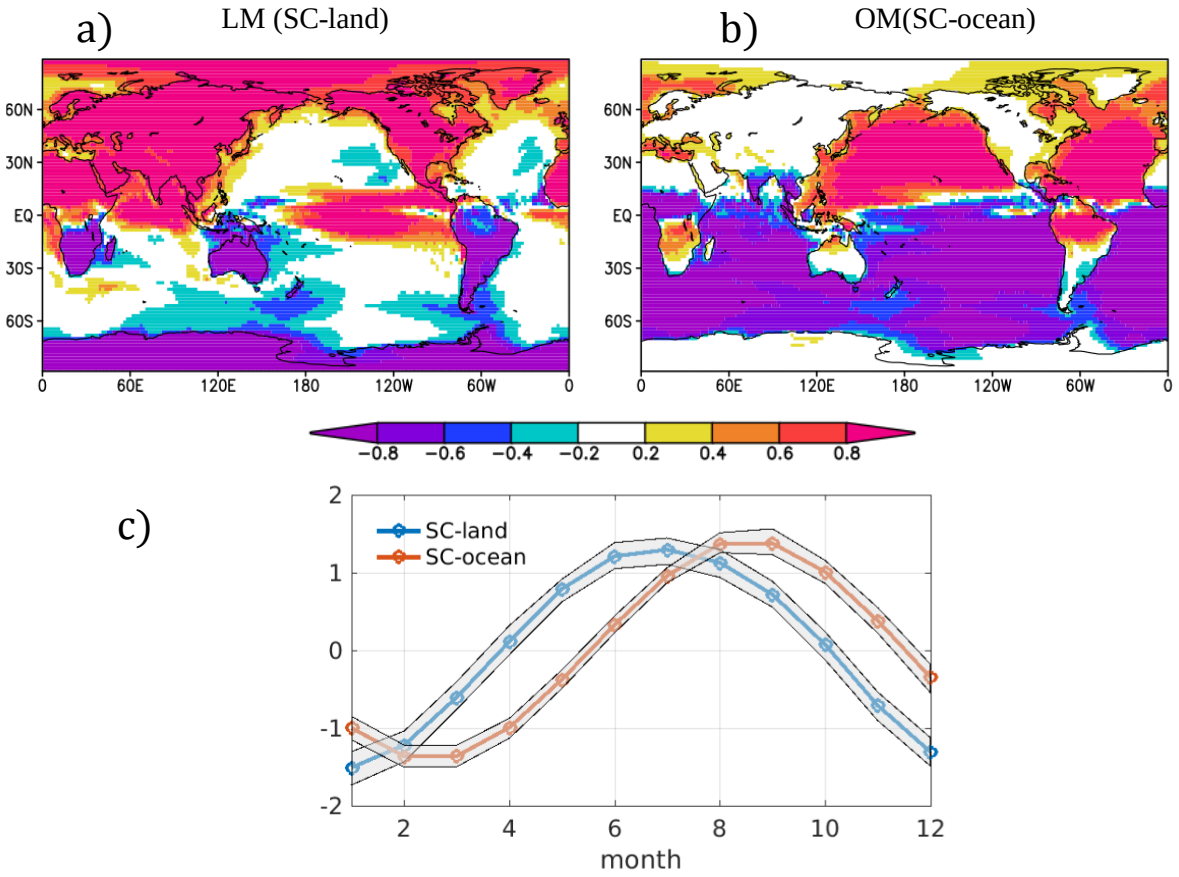

855

Accepted for publication in *Journal of Climate*. DOI10.1175/JCLI-D-20-0700.1.

Figure 3 (MPI-ESM-MR) a) Q-Q plot of the TM (IAC1) principal component: (upper panel: normal Q-Q plot; lower panel: residual Q-Q plot); b-c) Cross-correlations between PCs of TM (IAC1) and b) other IAC modes (IAC2: AM, IAC3: AAM, IAC4: TPM) and c) two seasonal modes. In b), horizontal dashed lines mark the 95% confidence intervals; in c) coefficients with P<0.01 are marked with squares; lag = -1corresponds to seasonal modes leading TM by 1 year; the climatological monthly cycle of two seasonal modes (blue: LM, 'SC-land', brown: OM, 'SC-ocean') follows right axis.

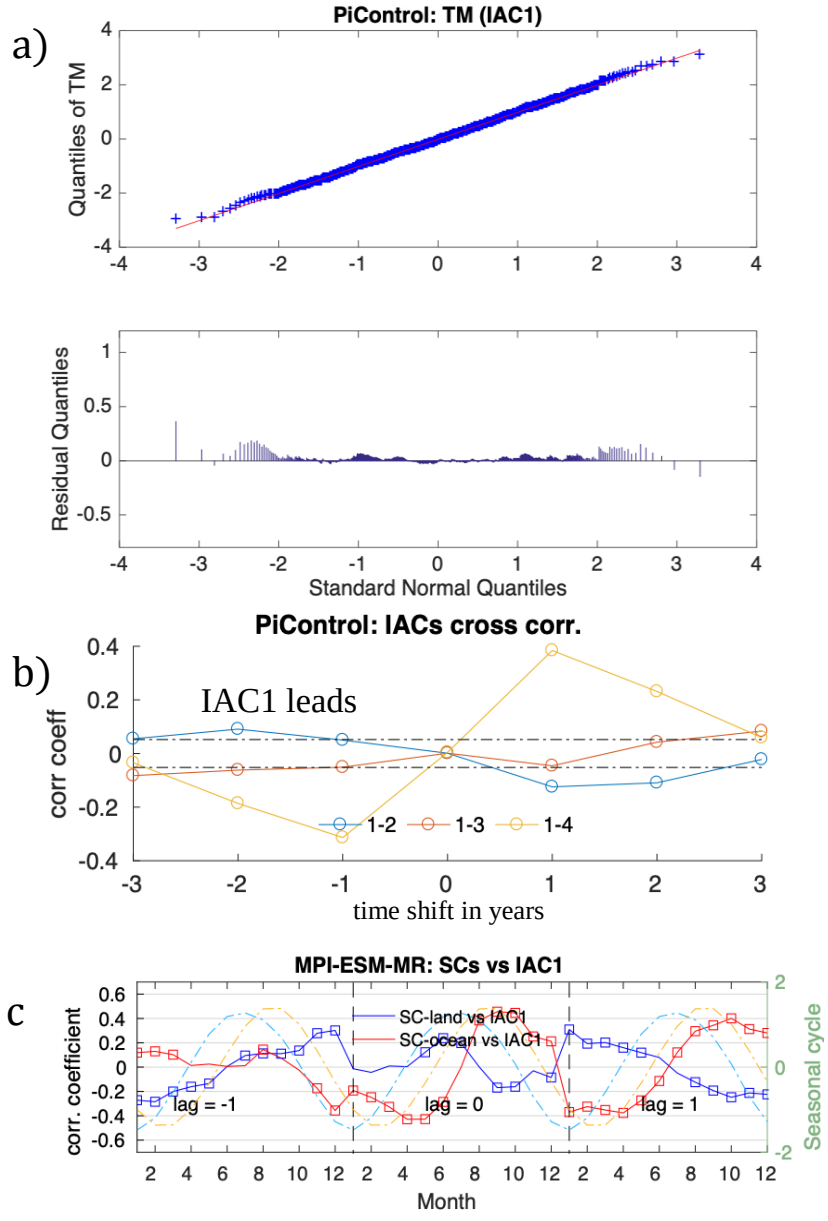

Accepted for publication in *Journal of Climate*. DOI10.1175/JCLI-D-20-0700.1.

Figure 4 (MPI-ESM-MR) Performance of candidate statistical models in terms of BIC (left axis) and r-squared (right axis) assessed in two steps; the top performer at each step is marked in gray. a) Three regression models: *SCs-only*, *IAC(1-4)-only*, and *SCs+IAC(1-4)* (the full model). b) Eight regression models, all including both SCs and TM(IAC1) but with different combinations of the other three IAC modes (IAC 2, 3, 4). The optimum regression model turns to be *SCs+IAC(1-2, 4)*. All candidate models comprising both SCs show their lowest BIC in December, thus m=12.

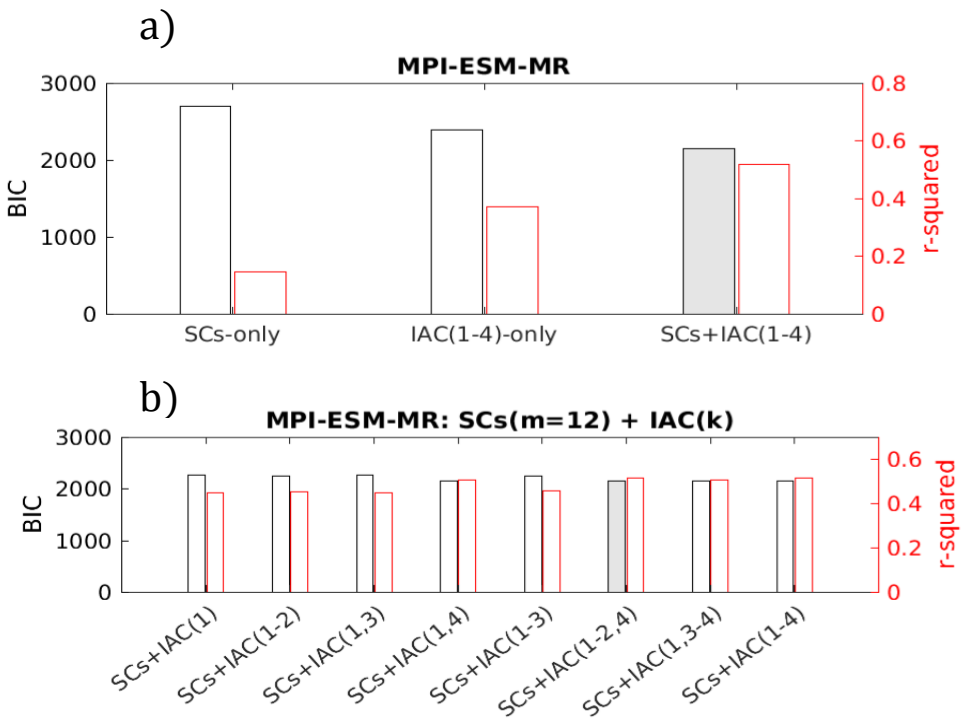

Accepted for publication in *Journal of Climate*. DOI10.1175/JCLI-D-20-0700.1.

Figure 5 (MPI-ESM-MR) Cross-validation of the optimum regression model for the PiControl simulation, with parameters determined from the first 500 years of TM's principle component (listed in Table 2), while the rest 500-yr data serves as the target holdout data (black), with respect to which predictions (red) are compared. Correlation between the holdout data and predictions is 0.74.

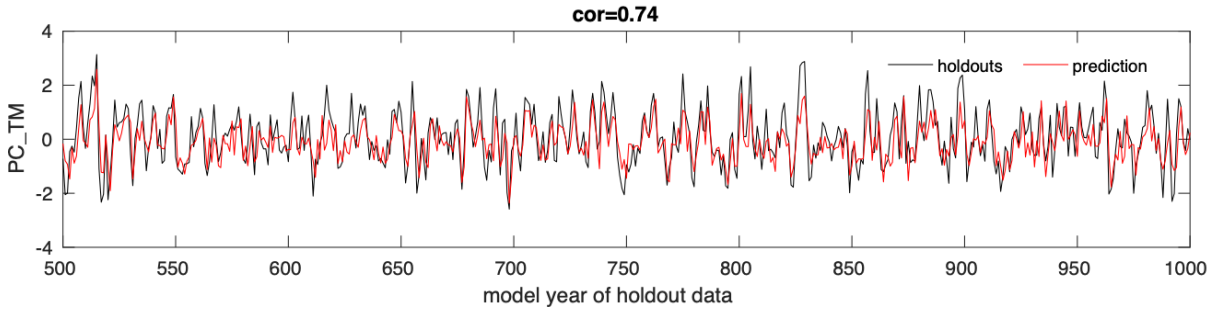

Accepted for publication in *Journal of Climate*. DOI10.1175/JCLI-D-20-0700.1.

892 Figure 6: (Multi-models) same as Fig.3 but for NCAR-CCSM4(a-c), IPSL-CM5A-R(d-f), MRI-

893 CGCM3(g-i), and GISS-E2-R(j-l). Only residual QQ plots are shown. The null hypothesis that TM

894 follows normal distribution is rejected in a) and j) ($p<0.01$, in both AD test and JB test).

895

896

897

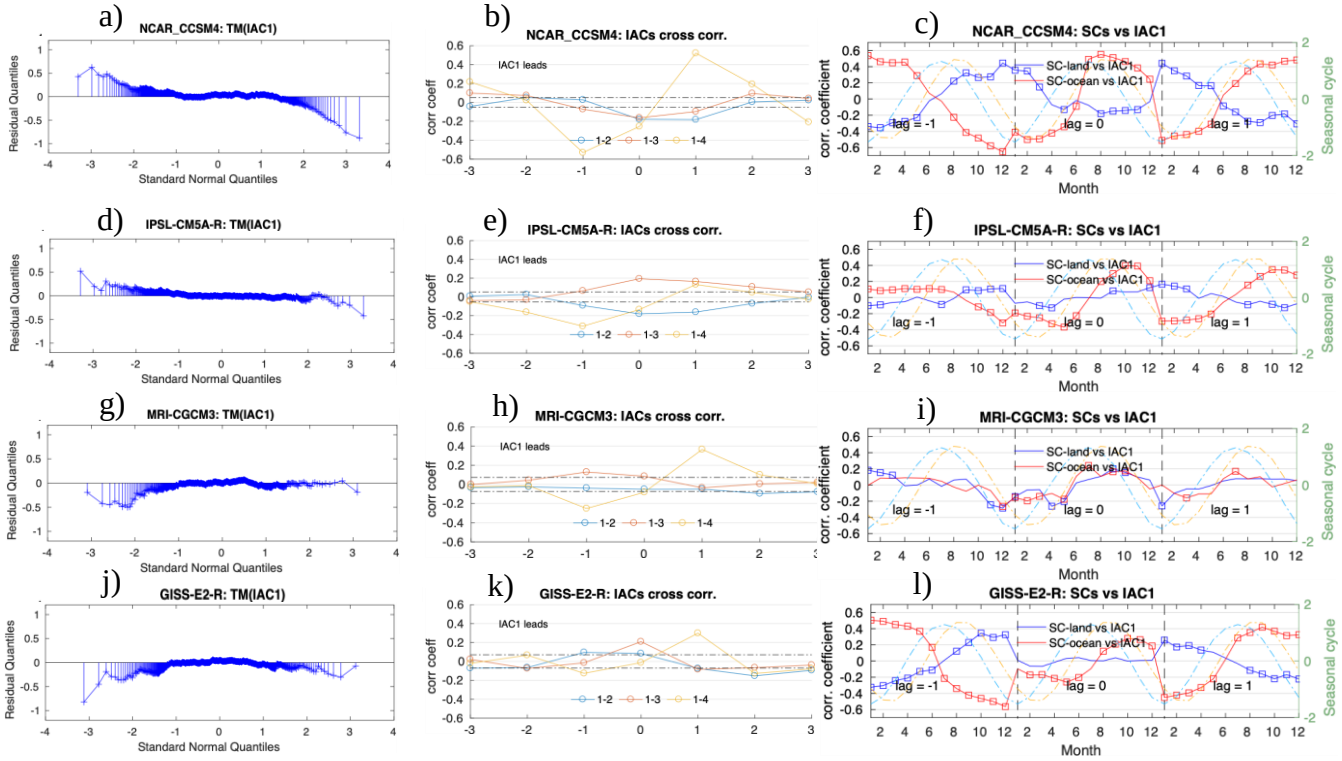

Accepted for publication in *Journal of Climate*. DOI10.1175/JCLI-D-20-0700.1.

Figure 7 (Multi-models) same as Figure 4a but including the optimum regression model in the last column (marked in gray). All regression models comprising seasonal components as explanatory variables have their best performances in December (m=12).

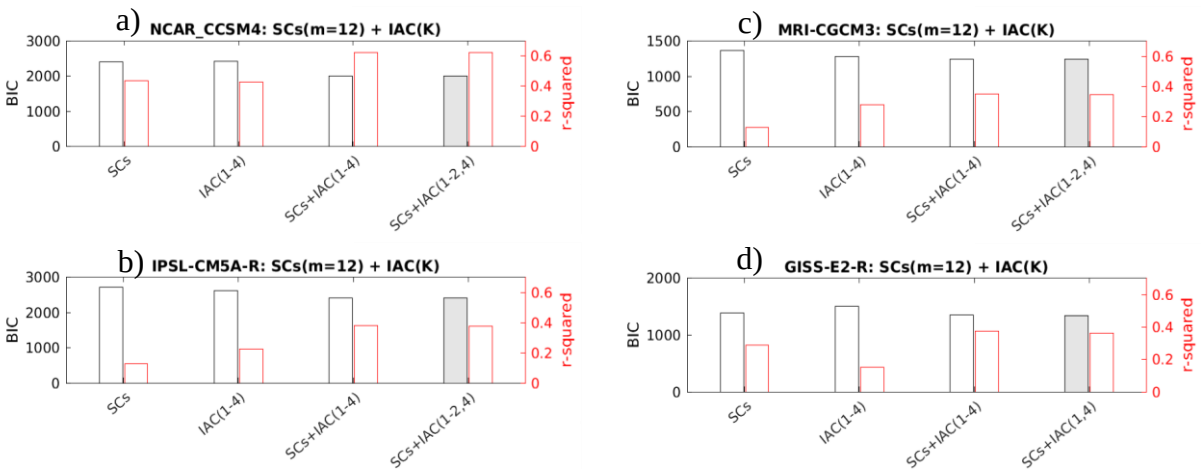

Accepted for publication in *Journal of Climate*. DOI10.1175/JCLI-D-20-0700.1.